



Bismuth-based metal-organic framework peroxidase-mimic nanzyme: Preparation and mechanism for colorimetric-converted ultra-trace electrochemical sensing of chromium ion



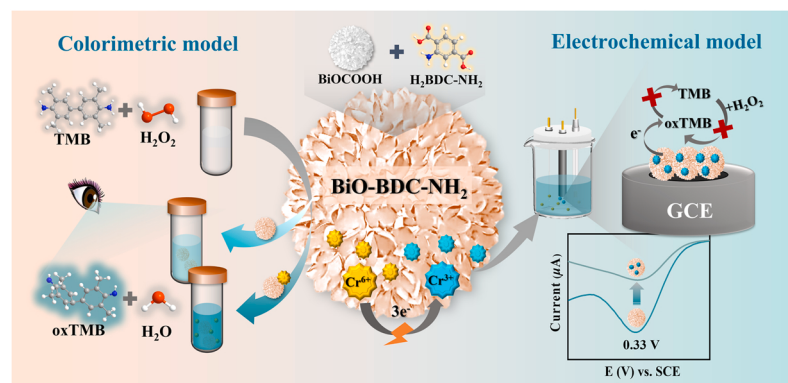
Qiu-Yu Yang, Chao-Qun Wan, Yu-Xin Wang, Xiao-Fang Shen, Yue-Hong Pang^{*}

State Key Laboratory of Food Science and Technology, School of Food Science and Technology, Jiangnan University, Wuxi 214122, China

HIGHLIGHTS

- A bismuth-based MOF nanzyme with 3D ball-flower shape was constructed.
- The MOF showed Cr⁶⁺-promoted and Cr³⁺-inhibited peroxidase-mimic activity.
- A dual-model colorimetric-electrochemical sensor for trace to ultra-trace Cr⁶⁺ detection.
- The colorimetric model can convert into sensitive electrochemical model.

GRAPHICAL ABSTRACT



ARTICLE INFO

Editor: Haizhou Liu

Keywords:
Nanzyme
Electrochemical/colorimetric sensor
Bismuth
Metal-organic framework
Chromium ion

ABSTRACT

A colorimetric-electrochemical dual-mode analytical method based on bismuth metal-organic framework nanzyme was developed for label-free and trace/ultra-trace Cr⁶⁺ detection. 3D ball-flower shaped bismuth oxide formate (BiOCOOH) was used as the precursor and template to facilely construct the metal-organic framework nanzyme BiO-BDC-NH₂, which possesses intrinsic peroxidase-mimic activity to effectively catalyze the colorless 3,3',5,5'-tetramethylbenzidine into blue oxidation products in the presence of hydrogen peroxide. Based on Cr⁶⁺ to promote the peroxide-mimic activity of BiO-BDC-NH₂ nanzyme, a colorimetric method for Cr⁶⁺ detection was developed with the detection limit of 0.44 ng mL⁻¹. Cr⁶⁺ can be electrochemically reduced to Cr³⁺ that would specifically inhibit the peroxidase-mimic activity of BiO-BDC-NH₂ nanzyme. Thus, the colorimetric system for Cr⁶⁺ detection was converted into a low-toxic and signal-off electrochemical sensor. The electrochemical model showed upgraded sensitivity and a lower detection limit of 9.00 pg mL⁻¹. The dual-model method was developed for selective appropriate sensing instruments in different detection scenarios, which can provide built-in correction for environmental effects, as well as the development and utilization of dual-signal sensing platforms for trace to ultra-trace Cr⁶⁺ rapid assay.

* Corresponding author.

E-mail address: yhpang@jiangnan.edu.cn (Y.-H. Pang).

1. Introduction

Heavy metal pollution was a detrimental outgrowth of growing industrialization and technological development. Non-biodegradable heavy metal ions discharged into the environment through industrial effluents and waste, led to irrigation and accumulation of sludge and sewage along the food chain, and ultimately resulted in chemical contamination of food threatening public health [31,47]. Among heavy metals, chromium (Cr) is a pervasive contamination due to its widespread utilization in metal plating, alloy smelting, battery and mining industries [16,28]. In particular, Cr⁶⁺ has been widely recognized as a human carcinogen with high mobility, substantial oxidizing properties and non-biodegradability, and 100 times higher toxicity than Cr³⁺ [26, 41]. Exposure to Cr⁶⁺ would increase the incidence of neurologic intoxication and the risk of developing lung and liver cancers [44]. Drinking water contaminated with Cr⁶⁺ presents the most widespread risk exposure, and the maximum permissible level of Cr⁶⁺ concentration set by the U.S. Environmental Protection Agency (EPA) and WHO is 0.05 mg L⁻¹ [21]. Given the conservation of environmental resources and the safety of the daily diet, it is clearly urgent to establish highly sensitive and effective strategies for Cr⁶⁺ determination.

During these decades, a wide variety of analytical approaches have been developed for Cr⁶⁺ assay, such as inductively coupled plasma mass spectrometry [32,33], atomic absorption spectrometry [6], ion chromatography [4,23], colorimetric method [12,24], electrochemical determination [16,27], Raman spectroscopy [38] and fluorescence spectroscopy [19]. The colorimetric method, based on the correlation between color intensity and/or hue and analyte concentration, has the advantages of visual measurement, portable device and convenient operation, which has become one of the most frequently used for laboratory test and on-site assay [12,50]. In particular, colorimetric sensing, based on enzyme mimic nanomaterials as nanozymes to catalyze chromogenic reaction, has become hot-spots due to its high sensitivity, visibility, label-free property, simplicity and cost-effectiveness [43].

Nanozymes with the advantages of comparatively high volume and stability, low cost, and convenient storage, have the potential as alternatives to natural enzymes [37]. Transition metal oxides [12], noble metals [51] and carbon nanomaterials [5] are the most conventional nanozyme species. The catalytic activity of nanozymes depends on the surface adsorption and electron transfer process [25]. Thus, nanomaterials with high surface area, adjustable organic structure and flexible nanoscale porosity, such as covalent-organic frameworks (COFs) [20,35], porous organic polymers [12] and metal-organic frameworks (MOFs) [18,49], have gained increasing attention due to their rational design capability to own ideal enzyme-mimic activities. In particular, MOFs are unique to tunable metal cavities as the active sites of the catalytic reaction, and the diverse and ordered porous structures for loading plenty of active metal sites, make it an ideal candidate material for nanozyme [30,53]. During these decades, the main group metals used in MOFs synthesis are constantly emerging due to their abundant resource, low environmental impact, and low cost [3]. Bi-based nanomaterials, such as bismuth oxide formate (BiOCOOH) and bismuth oxyhalides, have demonstrated high quantum efficiency, being used for photocatalysis, sensing and ionic conductivity [14,17]. Due to the coordination modes of metallic bismuth (Bi) and organic ligands with flexible geometric space, the synthesis of Bi-based MOFs with high catalytic efficiency as nanozyme has great potential in the development of highly sensitive sensing platform.

Dual-mode sensing platforms, based on two or more independent signal transduction, have been developed for more accurate quantitative determinations by reducing coexisting interference, operating or instrumental errors, and non-standard procedures [43,52]. In addition to colorimetric methods, electrochemical stripping analysis has been recognized as an important technology for heavy metal ions due to its remarkable sensitivity, low cost, and accurate determination at trace/ultra-trace levels [16,46]. While, it is crucial to design and prepare

a high-performance electrocatalyst and sensitive analytical method for Cr⁶⁺ detection. At present, the most widely studied electrochemical methods for Cr⁶⁺ detection are based on precious metal-based materials such as gold nanoparticles [34,36], and carbon or graphite nanomaterials [16,42]. The development of functional materials, which can be used for Cr⁶⁺ detection with favourable detection sensitivity and linear range, could promote the possibility of large-scale application. Therefore, the nanozyme modified electrochemical sensors effectively combine the earth-abundant electrocatalyst with excellent Cr⁶⁺ detection capability and high sensitivity electrochemical analysis. Improvingly, the conversion of the nanozyme colorimetric method into an electrochemical model can achieve detection at the ultra-trace level with a wide linear concentration range, and shorten the catalytic reaction time from ten or twenty minutes to tens of seconds [10]. Combining visualization and high sensitivity, the establishment of a colorimetric-electrochemical method can effectively improve the reliability of detection as well as the development of dual-signal devices for on-site rapid assays [20,52].

Herein, a dual-model colorimetric-electrochemical method based on MOF nanozyme derived from bismuth oxide formate (BiOCOOH) was developed for trace/ultra-trace Cr⁶⁺ detection. Three-dimensional BiOCOOH was used as the precursor and template for the fabrication of the ball-flower shaped metal-organic framework BiO-BDC-NH₂ nanozyme, which can effectively improve surface absorption and electronic transform performance. BiO-BDC-NH₂ nanozyme showed effective peroxidase-mimic activity to catalyze the conversion of the colorless 3,3',5,5'-tetramethylbenzidine (TMB) into blue oxidation products (oxTMB) in the presence of hydrogen peroxide (H₂O₂). The rapid and visual colorimetric analysis platform was converted into an electrochemical assay with obviously improved sensitivity and detection limit of Cr⁶⁺. The developed dual-model method provides a built-in correction to improve detection reliability and can be adapted to detect trace to ultra-trace in a wide linear range and different application scenarios, and the development of corresponding devices or sensing platforms has great potential for rapid on-site assays.

2. Experimental

2.1. Synthesis of nanozyme BiO-BDC-NH₂

BiO-BDC-NH₂ was synthesized by a two-step solvothermal method. The bismuth oxide formate (BiOCOOH) was synthesized using previously reported methods with slight improvement [7,15]. Bi(NO₃)₃•5 H₂O (2.00 mmol) was ultrasonically dispersed in 40 mL mixed solution (DMF:glycerine:H₂O=5:12:3, v/v/v). Then sealed the solution in a 50 mL Teflon-lined stainless-steel autoclave, maintained at 120 °C for 48 h and cooled down to room temperature. BiOCOOH as-synthesized was rinsed with ultrapure water and ethanol abstersion by centrifugal separation, and dried at 60 °C under vacuum overnight. BiOCOOH (0.4 mmol) and NH₂-H₂BDC (0.2 mmol) were ultrasonically dissolved in 20 mL mixed solution (DMF:methanol =4:1, v/v). The mixture was then transferred to a 25 mL Teflon-lined stainless-steel autoclave and heated at 120 °C for 48 h. The prepared product was collected by three consecutive washing/centrifugation cycles with DMF, acetone and ethanol. Finally, BiO-BDC-NH₂ was obtained and dried in vacuum at 70 °C.

2.2. Preparation of BiO-BDC-NH₂/GCE and reaction system

A traditional three-electrode system was adopted consisting of the working electrode of the modified glassy carbon electrode (GCE), Pt wire counter electrode and saturated calomel electrode (SCE) as the reference electrode. Bare GCE was polished sequentially on suede with 3 μm Al₂O₃ slurry and ultrasonic cleaning, then dried with nitrogen for later use. 5 μL BiO-BDC-NH₂ aqueous was dripped modified on the GCE surface until completely dried to form BiO-BDC-NH₂/GCE. The catalytic

reaction was tested in a 0.10 mol L⁻¹ acetate buffer system (ABS) containing TMB ethanol solution and H₂O₂ aqueous solution.

2.3. Electrochemical and colorimetric detection

Cyclic voltammetry (CV) was tested for potential from -0.20 V to -0.60 V in a redox probe of 0.10 mmol L⁻¹ [Fe(CN)₆]^{3-/4-} dissolved in 0.10 mol L⁻¹ pH 7.0 phosphate buffer solution (PBS, with 0.20 mol L⁻¹ KCl). Electrochemical impedance spectroscopy (EIS) was performed at a frequency of 0.01 Hz–100 kHz and a signal amplitude of 5.00 mV. The colorimetric detection was performed via UV-vis absorption spectra using BiO-BDC-NH₂ as a nanzyme in 0.10 mol L⁻¹ ABS (pH 4.0) and TMB and H₂O₂ with optimal concentration. Quantitative and standardized detection of Cr⁶⁺ was obtained by reading the absorbance value at 652 nm for optimal reaction time at room temperature. The electrochemical detection was electrochemically deposited Cr⁶⁺ on BiO-BDC-NH₂/GCE at -0.10 V for 120 s for accumulation, then performed by differential pulse voltammetry (DPV) in the system of 0.10 mol L⁻¹ ABS (pH 4.0), TMB and H₂O₂, with a potential range of 0.20–0.60 V, pulse width of 50 ms, and amplitude of 50 mV. The colorimetric and electrochemical method for Cr⁶⁺ detection was validated with respect to linearity, range, selectivity, repeatability and stability. The detection limit (LOD) was calculated using the mean intensity (*n* = 3) of the blank control (without Cr⁶⁺) plus three times of the standard deviation value. The mean, standard deviation, recovery (RSD), slope and y-intercept and correlation coefficient for the method validation characteristics were calculated by Origin and Microsoft Office Excel.

2.4. Peroxidase nanzyme catalytic kinetics

The peroxidase-mimic kinetic parameters of BiO-BDC-NH₂ nanzyme were carried out by measuring the change of the enzymological active with the independently changing concentrations of the TMB and H₂O₂ substrate according to the Lineweaver-Burk equation [11]:

$$\frac{1}{V} = \frac{K_m}{V_{\max}} \times \frac{1}{[C]} + \frac{1}{V_{\max}} \quad (1)$$

Where *V* refers to the initial velocity, *K_m* is the Michaelis-Menten constant, *V_{max}* is the maximum reaction velocity, *[C]* is the concentration of TMB/H₂O₂ substrate.

The Michaelis-Menten constant of the electrochemical model of BiO-BDC-NH₂ nanzyme was calculated by the Lineweaver-Burk equation 22:

$$\frac{1}{I_s} = \frac{K_m}{I_{\max}} \times \frac{1}{[C]} + \frac{1}{I_{\max}} \quad (2)$$

Where *I_s* represents the steady-state current after each addition of TMB substrate, *I_{max}* is the maximum current, *[C]* is the cumulative concentration of TMB in system.

2.5. Real sample preparation

Environmental samples including drinking water, tap water, lake water and soil were selected to verify the developed method by recovery calculation of Cr⁶⁺ spike samples. Drinking water was purchased from the local market, tap water was sampled in the laboratory and lake water was obtained from Li Lake at Jiangnan University and prepared by filtering through aqueous cellulose membrane. The soil sample was collected on campus, which was rinsed with deionized water and dried at 70 °C overnight, then ground into granules and weighed 0.1 g. Liquid samples were measured directly at 0.1 mL. Each sample, 5 mL concentrated nitric acid and 1 mL 30% hydrogen peroxide solution were added to the digestion tube and remained overnight. The samples were decomposed in a microwave digestion apparatus and then transferred to a graphite furnace to allow the solution to evaporate until almost dry. All

samples were diluted with deionized water.

3. Results and discussion

3.1. Structural characterization of BiO-BDC-NH₂ nanzyme

BiO-BDC-NH₂ nanzyme was synthesized based on the BiOCOOH precursor and template (Fig. 1A). Scanning electron microscopy (SEM) characterized the micromorphology of BiOCOOH and BiO-BDC-NH₂. Fig. 1B shows the 3D ball-flower shaped BiOCOOH with diameters of about 2–3 μm. A single BiOCOOH architecture consisted of several hundreds of nanosheets with smooth surfaces. As expected, BiO-BDC-NH₂ maintained the same 2D nanosheet structures and ball-flower architecture (Fig. 1C). While the nanosheets are inhomogeneous and fragmentary, a number of structures were dispersed after NH₂-H₂BDC binding. The N₂ adsorption-desorption isotherms of BiOCOOH and BiO-BDC-NH₂ were determined (Fig. 1D). The BET surface area (S_{BET}) was 32.72 m² g⁻¹ for BiOCOOH and 32.18 m² g⁻¹ for BiO-BDC-NH₂, and the Langmuir surface area (S_{Langmuir}) was 150.6 m² g⁻¹ and 159.0 m² g⁻¹, respectively. The mean pore size of BiOCOOH and BiO-BDC-NH₂ was 16.78 nm and 20.08 nm, respectively. The pore size distributions of BiOCOOH and BiO-BDC-NH₂ indicated that both contained a large number of mesopores (Fig. S1). The most widely distributed pore size of BiOCOOH was about 2–4 nm. As for BiO-BDC-NH₂, the number of 2–4 nm pores were obviously reduced and a relatively sharp peak was observed around 30.5 nm, suggesting the enlarged pore size after interaction with NH₂-H₂BDC.

The chemical construction of BiOCOOH and BiO-BDC-NH₂ was further characterized by Fourier transform infrared (FT-IR) spectrometry (Fig. 1E). Compared with BiOCOOH, the strong broad peak of -COOH at 2811 cm⁻¹ decreased and the stretching vibration of N-H peak at 3440 cm⁻¹ appeared, further revealing that the formation of BiO-BDC-NH₂ was due to the partial substitution of -COOH in BiOCOOH by NH₂-H₂BDC. Bi-O vibration was observed at 569 cm⁻¹ for BiOCOOH and 565 cm⁻¹ for BiO-BDC-NH₂ [15]. X-ray diffraction (XRD) profiles of BiOCOOH and BiO-BDC-NH₂ (Fig. 1F) are highly consistent and suggest that the fabricated nanoflowers were well-crystallized, which were manifested by unambiguous diffraction peaks at 24.3°, 28.8°, 32.5°, 33.7°, 35.1°, 35.1°, 46.5°, 53.5° and 55.7°, consistent with (101), (102), (110), (110), (103), (104), (200), (211) and (212) crystal planes of BiOCOOH (JCPDS Card No.35-0939) [7].

X-ray photoelectron spectroscopy (XPS) disclosed the surface chemical states and electronic structure of BiOCOOH and BiO-BDC-NH₂. Both contain Bi, C and O elements, in particular BiO-BDC-NH₂ possesses N elements derived from NH₂-H₂BDC (Fig. 1G). Double peaks in the 156.0–168.0 eV range were ascribed to Bi 4f, and peaks around 284.8 eV, 399.8 eV, and 532.0 eV were C 1s, N 1s, and O 1s, respectively. The high-resolution XPS spectra of Bi 4f normally showed two characteristic peaks for Bi 4f_{7/2} and Bi 4f_{5/2} species centered at 159.3 eV (BiOCOOH)/159.4 eV (BiO-BDC-NH₂) and 164.6 eV (BiOCOOH)/164.7 eV (BiO-BDC-NH₂), respectively, indicating that the Bi element mainly exists in the form of Bi³⁺ (Fig. 1H). The O 1s spectra can be deconvoluted into three characteristic features of Bi-O, C-O and C=O bonds, which peak at 530.0 eV, 531.6 eV and 532.8 eV for BiOCOOH, corresponding to 530.3 eV, 531.9 eV and 533.3 eV for BiO-BDC-NH₂ (Fig. 1I). Compared with BiOCOOH, BiO-BDC-NH₂ showed a decrease in the intensity of the Bi-O bond and an increase in the intensity of the C=O bond, indicating the enlarged organic component due to the combination of NH₂-H₂BDC. The high magnified N 1s spectrum of BiO-BDC-NH₂ peaks at 399.8 eV for -NH₂ (Fig. 1J). XPS results further revealed that the formation of BiO-BDC-NH₂ was incomplete/partial substitution reaction between NH₂-H₂BDC and the carboxyl functional groups of BiOCOOH, and the Bi-O combination was retained as the metal center of BiO-BDC-NH₂ nanzyme.

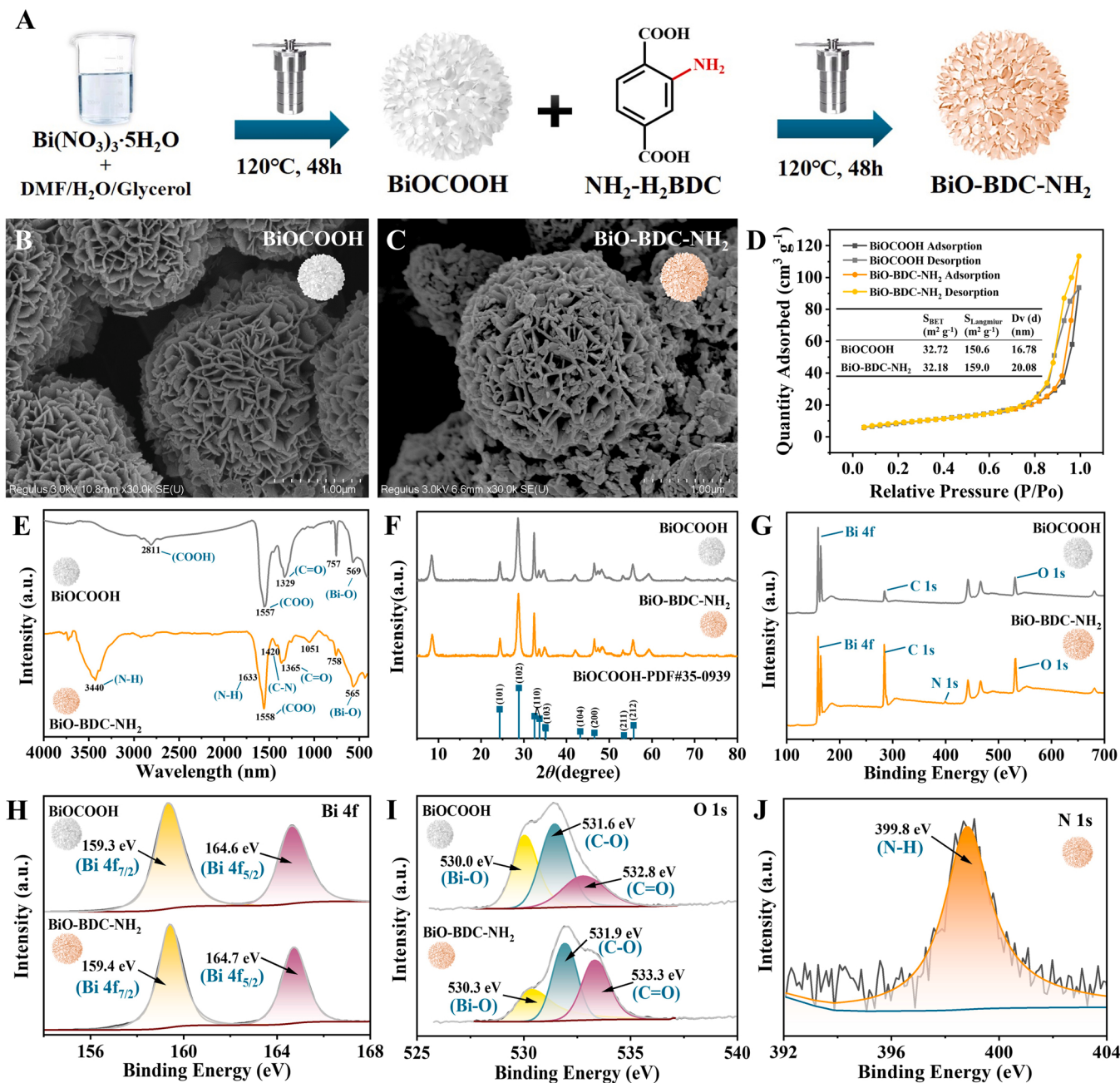


Fig. 1. (A) Schematic illustration of the preparation of BiO-BDC-NH₂. The SEM images of (B) BiOCOOH and (C) BiO-BDC-NH₂. (D) N₂ adsorption–desorption isotherms of BiOCOOH and BiO-BDC-NH₂. (E) FT-IR spectra and (F) XRD patterns of BiOCOOH and BiO-BDC-NH₂. (G) XPS survey spectra and narrow scan spectra of (H) Bi 4f, (I) O 1s of BiOCOOH and BiO-BDC-NH₂, and narrow scan spectra of (J) N 1s of BiO-BDC-NH₂.

3.2. Optical and electrochemical properties of BiO-BDC-NH₂ nanozyme

Digital imaging of 1.0 mg mL⁻¹ aqueous dispersion of BiOCOOH was white. After interaction with NH₂-H₂BDC, the 1.0 mg mL⁻¹ BiO-BDC-NH₂ aqueous turned to light orange (inset of Fig. 2A). Under ultraviolet illumination with a wavelength of 365 nm, the obvious blue fluorescence of BiO-BDC-NH₂ was visible to the naked eye, whereas this was not observed in BiOCOOH. The fluorescence emission spectra of suspension NH₂-H₂BDC, BiOCOOH and BiO-BDC-NH₂ were measured at 284 nm excitation wavelength (Fig. 2A). The distinguish feature peak of BiOCOOH was absent. NH₂-H₂BDC has a strong emission centered at 409 nm. In contrast, BiO-BDC-NH₂ exhibited significantly enhanced fluorescence at 432 nm a 23 nm redshift compared to NH₂-H₂BDC, due to an increase in the molar absorption coefficient of the fluorescent

substance by increasing the degree of conjugation of the system after introduction of NH₂-H₂BDC. The UV absorption spectra of BiOCOOH, BiO-BDC-NH₂ and NH₂-H₂BDC were further investigated (Fig. 2B). The optical absorption of BiO-BDC-NH₂ centered at a wavelength of ~349 nm was attributed to $\pi \rightarrow \pi^*$ and $n \rightarrow \pi^*$ transitions characterizing the aromatic compound and amidogen counterparts. Compared with the relative optical absorption of NH₂-H₂BDC at ~335 nm, a certain degree of redshift occurred due to the formation of a larger conjugated group of BiO-BDC-NH₂. To sum up, the substitution of NH₂-H₂BDC introduced an enlarged conjugation system into BiOCOOH, resulting in BiO-BDC-NH₂ with improved electronic transmission and catalytic sensitivity.

Cyclic voltammetry (CV) (scan rate: 50 mV s⁻¹) (Fig. 2C) and electrochemical impedance spectroscopy (EIS) (Fig. 2D) were investigated in $[\text{Fe}(\text{CN})_6]^{3-/4-}$ redox probe on BiOCOOH and BiO-BDC-NH₂ modified

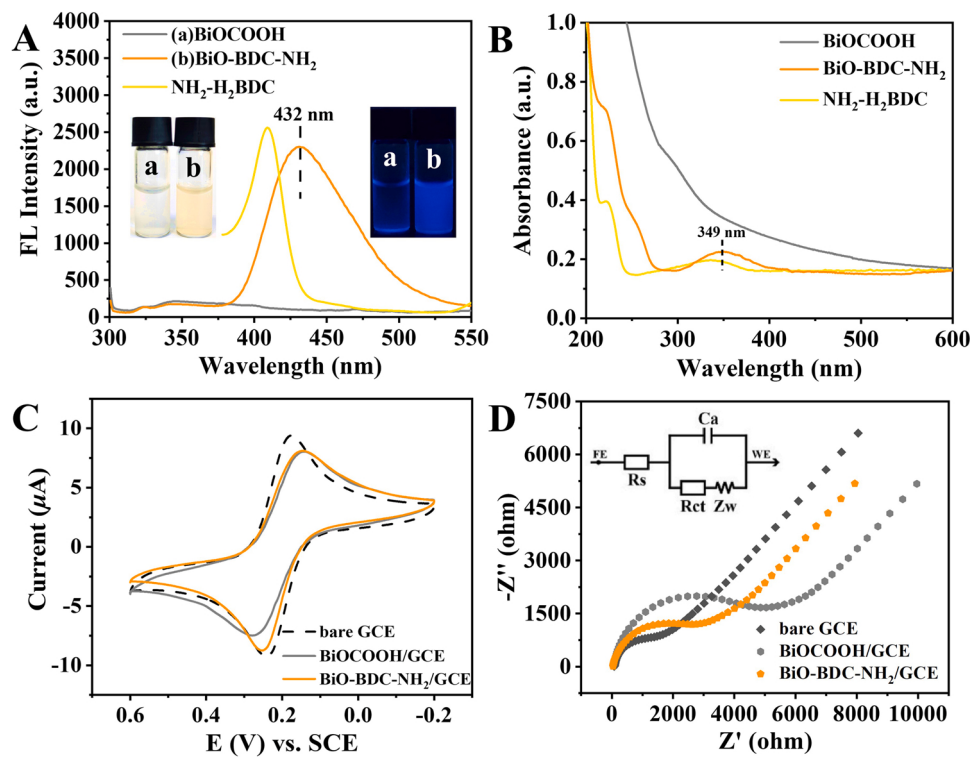


Fig. 2. (A) Fluorescence spectra (Insert plots: digital photo and its under ultraviolet illumination with a wavelength of 365 nm) and (B) UV–vis absorption spectra of 1.0 mg mL⁻¹ aqueous dispersion of NH₂-H₂BDC, BiOCOOH and BiO-BDC-NH₂. (C) CV and (D) EIS curves of bare GCE, BiOCOOH/ GCE and BiO-BDC-NH₂/ GCE in 1.0 mmol L⁻¹ [Fe(CN)₆]^{3-/4-} (+0.2 mol L⁻¹ KCl) (Scan rate of CV: 50 mV s⁻¹).

GCE. For bare GCE, a pair of well-defined quasi-reversible redox peaks of Fe²⁺/Fe³⁺ redox pairs were obtained, in which the anodic current (I_{pa}) was $-9.86 \mu\text{A}$ and the cathodic current (I_{pc}) was $9.73 \mu\text{A}$. After modified with BiOCOOH, I_{pa} and I_{pc} decreased to $-7.85 \mu\text{A}$ and $7.60 \mu\text{A}$, respectively. The I_{pa} and I_{pc} of BiO-BDC-NH₂/GCE were $-9.68 \mu\text{A}$ and $8.21 \mu\text{A}$, both of which had less reduction than BiOCOOH. Meanwhile, the potential difference between anodic and cathodic peak (ΔE_p) increased from 0.07 V (bare GCE) to 0.14 V (BiOCOOH/GCE) and 0.11 V (BiO-BDC-NH₂/GCE), respectively. The reduced electrical conductivity was probably caused by the introduction of organic components. BiO-BDC-NH₂ showed better electrostatic attraction and electron diffusion than BiOCOOH.

The EIS of GCE, BiOCOOH/GCE and BiO-BDC-NH₂/GCE were synchronized with CV (Fig. 2D). The modification of BiOCOOH and BiO-BDC-NH₂ resulted in an increase in charge transfer resistance (Rct) from 1813Ω (bare GCE) to 5140Ω and 3022Ω , respectively. It is further indicated that BiO-BDC-NH₂ could facilitate the electron transfer process on the electrode surface, and process a higher conductivity performance than BiOCOOH.

The effective surface areas of BiOCOOH and BiO-BDC-NH₂ modified GCE were investigated by linearity between redox peak current and scan rate in [Fe(CN)₆]^{3-/4-} redox probe standard solution (Fig. S2). With the increase of the scan rate, the redox peak currents of Fe²⁺/Fe³⁺ redox couple on both BiOCOOH and BiO-BDC-NH₂ modified GCE gradually increased (Fig. S2A and C). The redox peak currents were linear with the square root of the scan rate, indicating that [Fe(CN)₆]^{3-/4-} on the modified electrode surface was governed by the diffusion condition (Fig. S2B and D). The effective surface areas of BiOCOOH/GCE and BiO-BDC-NH₂/GCE were calculated by Randles–Sevcik equation [29]:

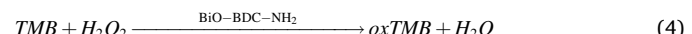
$$I_p = 268,600 ACD^{1/2} n^{2/3} \nu^{1/2} \quad (3)$$

Where, A refers to the effective surface area (cm²), C is the bulk concentration of [Fe(CN)₆]^{3-/4-} (mol cm⁻³), D is the diffusion coefficient ($7.60 \times 10^{-6} \text{ cm}^2 \text{ s}^{-1}$), n is the number of electrons transferred in the

redox event ($n = 1$), and ν is the scan rates (V s⁻¹) I_p is anodic peak current (A). The effective electrochemical surface area was calculated as 0.095 cm^2 for BiOCOOH/GCE and 0.124 cm^2 for BiO-BDC-NH₂/GCE, which was 1.34-fold and 1.75-fold of the bare GCE surface area (0.071 cm^2), respectively. Therefore, BiO-BDC-NH₂ has a larger specific capacitance and an increased electrochemical active surface area than BiOCOOH, which is beneficial for electron transfer and conductivity.

3.3. Colorimetric performance of BiO-BDC-NH₂ to Cr³⁺ and Cr⁶⁺

Peroxidase-mimic activity of BiOCOOH and BiO-BDC-NH₂ was assessed by oxidizing TMB with H₂O₂ (Fig. 3A). Under the same conditions, BiO-BDC-NH₂ (OD₆₅₂ = 0.873) showed superior catalytic activity towards TMB than BiOCOOH (OD₆₅₂ = 0.338). Significant differences in peroxidase mimics between these two nanomaterials were mainly caused by the introduction of conjugated organic components improving surface properties and electron transfer capabilities [40]. Control experiments of BiO-BDC-NH₂ +TMB, BiO-BDC-NH₂ +H₂O₂ and BiO-BDC-NH₂ +TMB+H₂O₂ were designed and reacted under the same conditions (Fig. 3B). From the absorption spectra, none other than the BiO-BDC-NH₂ +TMB+H₂O₂ system showed an extremely high UV absorption peak at 652 nm, indicating the intrinsic peroxidase-mimic activity of the prepared BiO-BDC-NH₂ nanozyme. In the presence of H₂O₂, BiO-BDC-NH₂ nanozyme can catalyze the conversion of chromogenic TMB substrate into oxidized blue-colored oxTMB product by the following equation:



The intervention of chromium ions into the BiO-BDC-NH₂ +TMB+H₂O₂ system was further investigated via UV–vis absorption spectra (Fig. 3C). When BiO-BDC-NH₂ nanozyme was incubated with Cr³⁺, an attenuated catalytic efficiency of BiO-BDC-NH₂ towards TMB was shown and the lake blue color of the solution faded to light blue (vial b). Conversely, with the addition of Cr⁶⁺, an increase in peroxidase-

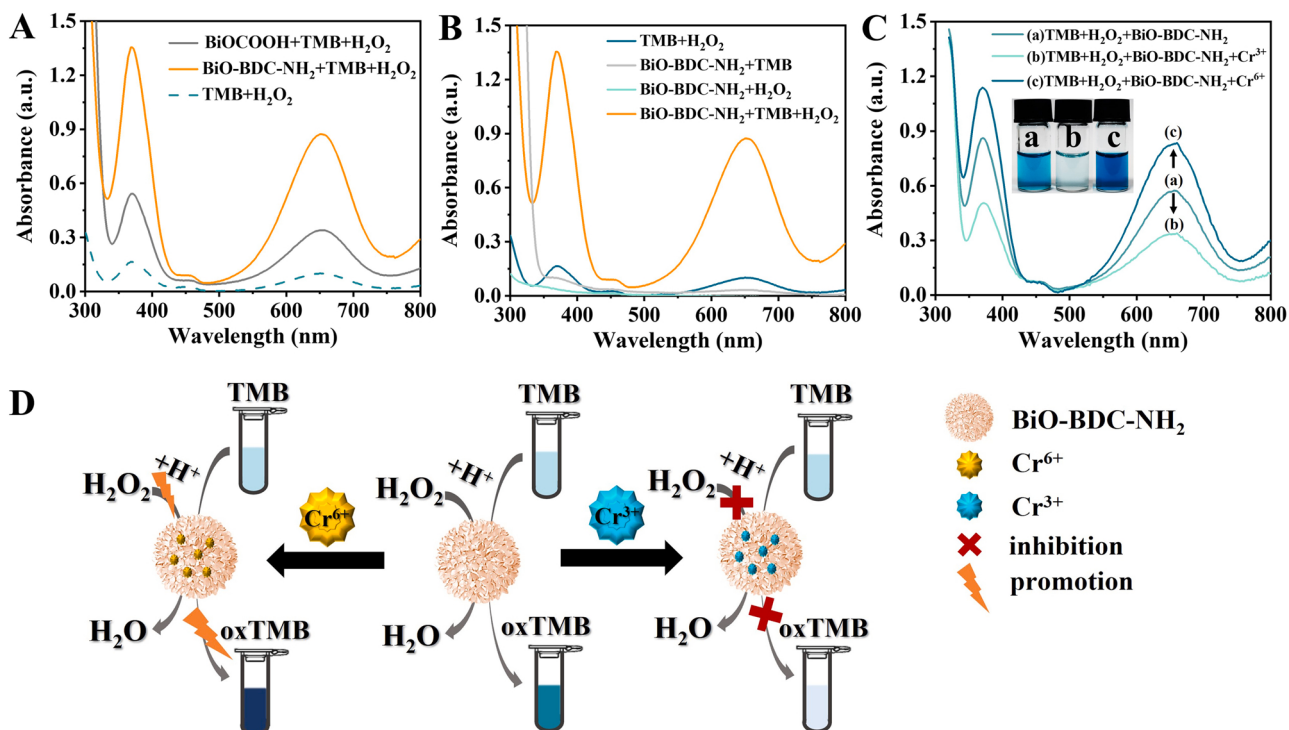


Fig. 3. (A) The comparison of peroxidase-like activity of BiOCOOH and BiO-BDC-NH₂ via UV–vis absorption spectra (0.10 mol L^{-1} ABS, pH 4.0). (B) Absorption spectral observation of BiO-BDC-NH₂ peroxidase-like activity. (C) UV–vis absorption spectra of the solutions of BiO-BDC-NH₂ + TMB + H₂O₂ system (0.10 mol L^{-1} ABS, pH 4.0) in the (a) absence and presence of 200 ng mL^{-1} (b) Cr³⁺ and (c) Cr⁶⁺. (Inset plots: Corresponding photographs). (D) Illustration of the colorimetric method of BiO-BDC-NH₂ nanozyme as a probe for chromium ions detection.

like activity was observed with the change in color from lake blue (vial a) to dark blue (vial c). The results suggested the feasibility of colorimetric determination of Cr³⁺/Cr⁶⁺ based on BiO-BDC-NH₂ sensing probe (Fig. 3D).

To optimize the detection conditions, pH of acetate buffer (ABS), reaction time, H₂O₂, TMB and BiO-BDC-NH₂ nanozyme concentrations were investigated. pH optimization of the BiO-BDC-NH₂ + TMB + H₂O₂ system was carried out at pH 3.0–6.0 in 0.10 mol L^{-1} ABS via UV–vis absorption spectra (Fig. S3A). From pH 3.0–4.0, UV absorption peaked at 652 nm (OD₆₅₂) and gradually increased to the maximum. As the pH increased further to 6.0, the absorption peak at 652 nm decreased sharply to zero. When the chromogenic system was in the presence of 200 ng mL^{-1} Cr³⁺ and Cr⁶⁺, the maximum difference values of OD₆₅₂ of both were shown at pH 4.0 (Fig. S3B and C). The apparent discrepancy of chromogenic reactions with the buffer system at different pH can be clearly observed in the photographs of Fig. S3D. The chromogenic reaction was more significant at pH 3.0–4.0 than at pH 4.5–6.0, due to the acid condition benefiting the production of hydroxyl radicals (•OH) by H₂O₂ [39]. Thus, pH 4.0 was the optimal pH response condition for the colorimetric BiO-BDC-NH₂ + TMB + H₂O₂ system.

To optimize the reaction time, changes in UV absorption peaks at 652 nm (ΔOD_{652}) over time of the BiO-BDC-NH₂ + TMB + H₂O₂ system with and without Cr³⁺/Cr⁶⁺ were monitored (Fig. S3E and F). With the increase of reaction time, the absorption of the catalytic reaction system was first increased and then ΔOD_{652} tended to be stable ($p > 0.05$) after 20 min for Cr³⁺ and 10 min for Cr⁶⁺, respectively. Herein, the reaction time was extended to 20 min for Cr³⁺ and 10 min for Cr⁶⁺ detection was beneficial for chromogenic reaction.

The concentration of each component of the catalyst system can strongly influence the chromogenic effect. OD₆₅₂ increased in the concentration range of $20.0\text{--}120 \text{ mmol L}^{-1}$ and reached a plateau when the concentration of H₂O₂ exceeded 80.0 mmol L^{-1} (Fig. S3G). The concentration of the chromogenic substrate TMB was optimized from 0.20 to 1.60 mmol L^{-1} , and the optimal concentration was 1.20 mmol L^{-1}

(Fig. S3H). With a crescent concentration of $0.02\text{--}0.10 \text{ mg mL}^{-1}$ for BiO-BDC-NH₂ nanozyme, the OD₆₅₂ of the chromogenic system increases and reaches a maximum of 0.08 mg mL^{-1} (Fig. S3I). The influence of temperature on the peroxidase-like activity of BiO-BDC-NH₂ nanozyme was studied, which showed good thermal stability after incubation at $4\text{--}90^\circ\text{C}$ for 30 min (Fig. S3J). Thus, the follow-up experiments were conducted at room temperature. To sum up, subsequent tests were carried out under optimal conditions (reaction system: 80.0 mmol L^{-1} of H₂O₂, 1.20 mmol L^{-1} of TMB and 0.08 mg mL^{-1} of BiO-BDC-NH₂, pH = 4.0; reaction time: 20 min for Cr³⁺ and 10 min for Cr⁶⁺).

Under optimized conditions, OD₆₅₂ of the BiO-BDC-NH₂ + TMB + H₂O₂ system before and after addition of Cr³⁺/Cr⁶⁺ were measured. When the added Cr⁶⁺ concentration increased from 0 to 1400 ng mL^{-1} , OD₆₅₂ of oxTMB increased and levelled at about 1200 ng mL^{-1} , and the blue color of the chromogenic system gradually darkened (Fig. 4A). The ΔOD_{652} increased linearly with the logarithmic concentration of Cr⁶⁺ ($\log C(\text{Cr}^{6+})$), and the following regression equation was obtained: $\Delta \text{OD}_{652} = -0.780 + 0.475 \log C(\text{Cr}^{6+})$ ($R^2 = 0.998$) with a linear range of $1.50\text{--}1400 \text{ ng mL}^{-1}$, yielding a detection limit (LOD) of 0.44 ng mL^{-1} (3 S/N) (Fig. 4B). With the addition of Cr³⁺ from 0 to 1000 ng mL^{-1} , the chromogenic system solutions gradually changed from apparently lake blue to near-colorless (Fig. S4A). The corresponding calibration plots were obtained with the linear equation $\Delta \text{OD}_{652} = -0.519 + 0.426 \log C(\text{Cr}^{3+})$ ($R^2 = 0.994$) and the linear range is $2.00\text{--}1000 \text{ ng mL}^{-1}$. Based on the narrow concentration, LOD was estimated at 0.56 ng mL^{-1} ($S/N = 3$) (Fig. S4B). LOD and linear ranges are comparable to or even better than most reported colorimetric methods based on different nanomaterials for chromium detection (Table S1). The digestion operation of the real sample pretreatment will oxidize the contained Cr³⁺ to Cr⁶⁺, so the application of the colorimetric method was in the form of Cr⁶⁺.

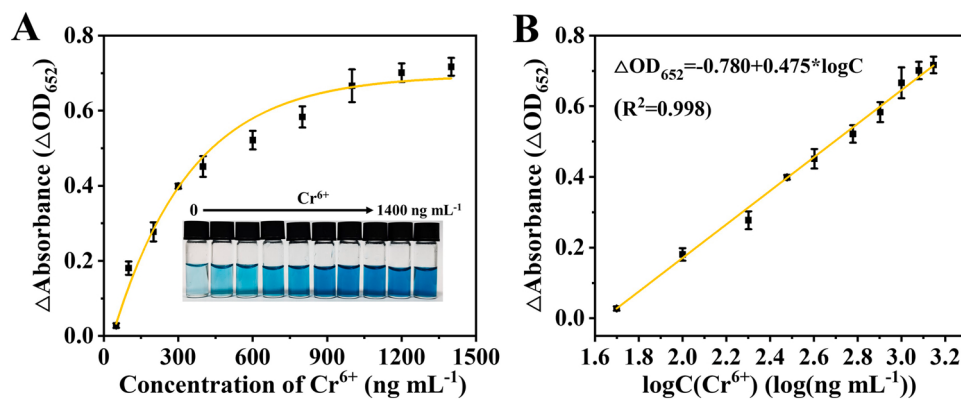


Fig. 4. (A) Linear relationship between ΔOD_{652} and the different concentrations of Cr^{6+} in the range from 0 to 1400 ng mL^{-1} (Inset plots: Corresponding photographs). (B) Calibration curve for $\log C(\text{Cr}^{6+})$ vs. ΔOD_{652} .

3.4. Mechanism analysis of BiO-BDC-NH₂ to Cr^{3+} and Cr^{6+}

To investigate the differential sensing mechanism of BiO-BDC-NH₂ towards Cr^{3+} and Cr^{6+} , XPS characterizations of samples were used to illustrate the interaction between BiO-BDC-NH₂ and $\text{Cr}^{3+}/\text{Cr}^{6+}$. The full-range XPS spectra of BiO-BDC-NH₂ before and after interaction with $\text{Cr}^{3+}/\text{Cr}^{6+}$ are shown in Fig. 5A. Peak values range from 570 eV to 595 eV of Cr 2p after adsorption of $\text{Cr}^{3+}/\text{Cr}^{6+}$ by BiO-BDC-NH₂. The Cr 2p high resolution XPS spectra represent chromium ion valence (Fig. 5B). As for Cr^{3+} , two characteristic peaks of Cr 2p_{3/2} and Cr 2p_{1/2} were shown at 577.0 eV and 586.7 eV. In comparison, the Cr 2p_{3/2} and Cr 2p_{1/2} characteristic peaks of Cr^{6+} centered at 579.0 eV and 588.3 eV, with two satellite peaks at 576.7 eV and 586.3 eV, respectively [45]. Bi 4f spectra for pristine BiO-BDC-NH₂ showed two peaks of Bi 4f_{7/2} and Bi 4f_{5/2} with binding energy of 159.4 eV and 164.7 eV, respectively. After interaction with $\text{Cr}^{3+}/\text{Cr}^{6+}$, these peaks shifted notably towards lower binding energy regions of 159.1 eV/158.3 eV and 164.4 eV/163.6 eV, suggesting an increase in the electron density of

BiO-BDC-NH₂ [13] (Fig. 5C).

O 1 s narrow scanning spectra revealed the difference in the interaction of BiO-BDC-NH₂ with Cr^{3+} and Cr^{6+} (Fig. 5D). The O 1 s spectrum of BiO-BDC-NH₂ was divided into three peaks at 530.3 eV, 531.9 eV and 533.3 eV, belonging to Bi–O, C–O and C=O, respectively. The introduction of $\text{Cr}^{3+}/\text{Cr}^{6+}$ leads to a lower binding energy shift at the O 1 s core level. After Cr^{3+} adsorption, the relative peak area of the Bi–O bond decreased substantially from 27.0% to 2.70%, indicating that the appended Cr^{3+} broke the Bi–O bond of BiO-BDC-NH₂, thus disabling its catalytic ability. By contrast, the applied Cr^{6+} resulted in an increase in the peak area of Bi–O to 56.4% and a decrease in the peak area of C–O and C=O, which verified the generation of Cr–O bond via electrostatic interaction on BiO-BDC-NH₂. In addition, both Cr^{3+} and Cr^{6+} allowed the N 1 s core level of BiO-BDC-NH₂ to shift to higher binding energy and the N–H peak area decreased, indicating that imine groups were involved in $\text{Cr}^{3+}/\text{Cr}^{6+}$ (Fig. 5E).

ζ potential characterizations were used to further characterize the disparate Cr^{3+} and Cr^{6+} reactions on BiO-BDC-NH₂ (Fig. 5F). The ζ

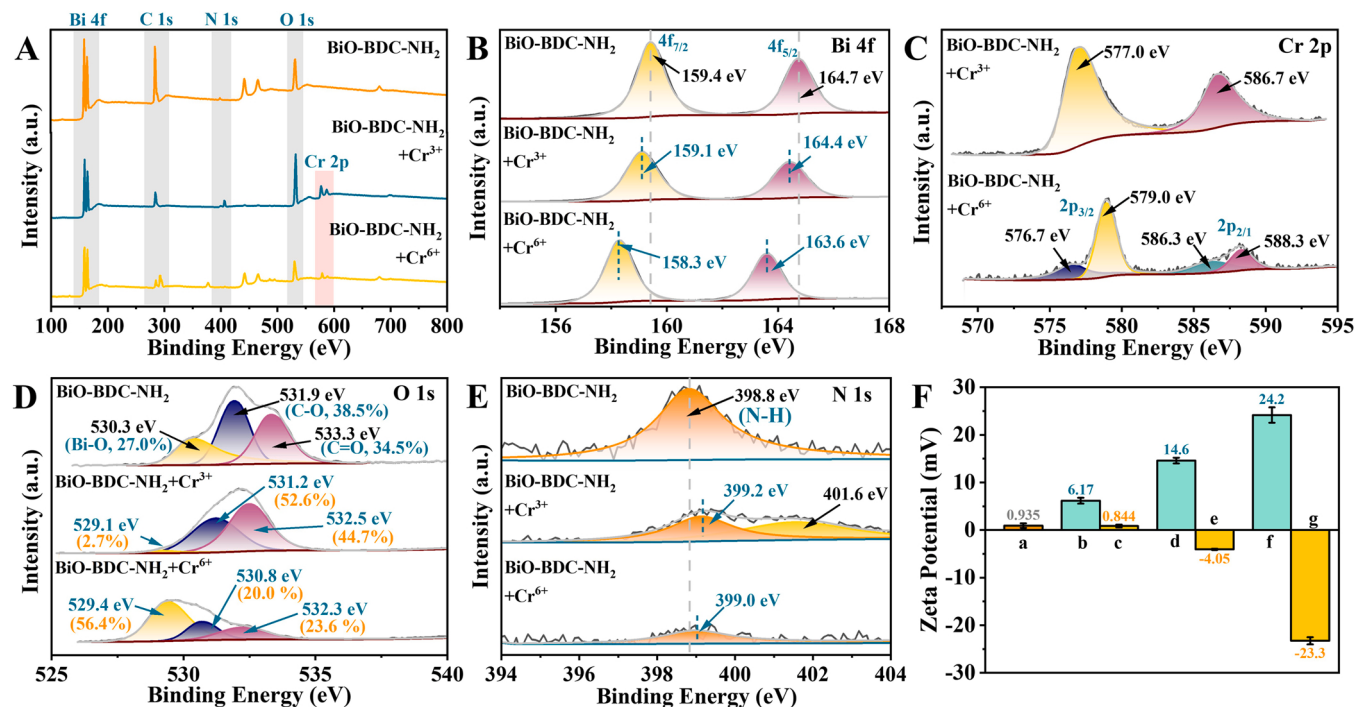


Fig. 5. (A) Full-range XPS survey spectra and narrow scan spectra of (B) Bi 4f, (C) Cr 2p, (D) O 1s and (E) N 1s of BiO-BDC-NH₂ with the addition of Cr^{3+} and Cr^{6+} . (F) Histogram of the ζ potential of (a) BiO-BDC-NH₂ and BiO-BDC-NH₂ incubated with 10 ng mL^{-1} (b) Cr^{3+} /c) Cr^{6+} , 100 ng mL^{-1} (d) Cr^{3+} /e) Cr^{6+} and 1000 ng mL^{-1} (f) Cr^{3+} /g) Cr^{6+} .

potential of BiO-BDC-NH₂ was measured to be 0.935 mV (column a). The amount of BiO-BDC-NH₂ positive surface charges increased to 6.17 mV with the addition of 10 ng mL⁻¹ Cr³⁺ at pH 4.0 (column b), and reduced to 0.844 mV of 10 ng mL⁻¹ Cr³⁺/Cr⁶⁺ (column c). When the incubation ion concentration increased to 100 ng mL⁻¹, the surface charge of BiO-BDC-NH₂ +Cr³⁺ increased to 14.6 mV (column d) and the potential of BiO-BDC-NH₂ +Cr⁶⁺ turned negative (-4.05 mV, column e). While the addition of 1000 ng mL⁻¹ Cr³⁺/Cr⁶⁺, the ζ potential remained positive/negative increased to 24.2 mV/-23.3 mV (column f/g). These changes could be explained by electrostatic repulsion and adsorption of BiO-BDC-NH₂ to positive Cr³⁺ and negative Cr⁶⁺ at pH 4.0.

3.5. Electrochemical detection of Cr⁶⁺ on BiO-BDC-NH₂/GCE

Electrochemical techniques have been widely used in the detection of trace/ultra-trace heavy metal ions. In general, the developed method is based on electrochemical active metal ions, controlling the redox reaction between metal elements and ions or different ion valences by potential regulation [30]. Although TMB as an electrochemically active molecule has already been applied to electrochemical assays of toxic targets in various fields, the design and application of TMB for electrochemical detection of metal ions is quite limited [2]. In addition, the adoption of nanomaterials with favorable catalytic efficiency to develop enzyme electrodes to replace electrochemical biosensors based on natural enzymes has become the trend [43]. It is of great significance to use efficient non-enzymatic electrocatalysts to achieve ultrasonic electrochemical assay. Therefore, the colorimetric method for Cr⁶⁺ detection was converted into an electrochemical assay based on BiO-BDC-NH₂ nanozyme modified GCE and the TMB+H₂O₂ substrate system (0.10 mol L⁻¹ ABS, pH 4.0).

BiOCOOH and BiO-BDC-NH₂ were dipping modified on GCE to oxidize TMB in the presence of H₂O₂ to evaluate peroxidase-mimic activity via CV (Fig. 6A). The bare GCE showed no response to the

TMB+H₂O₂ system. Compared with BiOCOOH/GCE, the CV response on BiO-BDC-NH₂/GCE showed two pairs of distinguishable redox peak currents, indicating that BiO-BDC-NH₂ possesses the preferred mimetic peroxidase catalysis due to the oxidation of the TMB+H₂O₂ system. To exclude interference with the peroxidase process, BiO-BDC-NH₂/GCE control experiments oxidized H₂O₂, TMB and TMB+H₂O₂ substrates by CV (Fig. 6B). For H₂O₂, the redox peak was not apparent. In the TMB substrate, two pairs of redox peaks appeared attributed to oxTMB generation. When both TMB and H₂O₂ existed, well-defined quasi-reversible redox peaks of oxTMB were observed, demonstrating the more significant peroxidase-like activity of BiO-BDC-NH₂ nanozyme than oxidase activity.

The electrochemical performance of Cr³⁺ and Cr⁶⁺ were characterized via CV in the potential range of -0.60 – 1.00 V at a scan rate of 50 mV s⁻¹ in 0.10 mol L⁻¹ ABS (pH 4.0) (Fig. 6C). As for Cr³⁺, the obtuse redox peaks obtained around 0.01 V. The only well-shaped response peak current is 0.02 V, ascribed as the characteristic peak of Cr⁶⁺ reduced Cr³⁺. In the reported research, the oxidation peak potential of Cr⁰ to Cr³⁺ is -0.84 V [8]. Therefore, within the potential range of 0.20 – 0.60 V for oxTMB representation, interference due to electrochemical redox reactions of chromium ions would not be involved. Based on these, the pretreatment strategy was set to stay at -0.10 V and maintain 120 s for the reduction of Cr⁶⁺–Cr³⁺, as well as the accumulation and interaction of Cr³⁺ on electrode surface. Differential pulse voltammetry (DPV) was applied to illustrate the electrochemical sensing feasibility of Cr⁶⁺ (Fig. 6D). In the absence of Cr⁶⁺, oxTMB exhibited distinct oxidation peaks at the potentials of 0.33 V and 0.48 V on BiO-BDC-NH₂/GCE. After pretreatment progress, DPV responses showed a decrease in peak currents with increased Cr⁶⁺ concentration, due to Cr³⁺ reduced by Cr⁶⁺ inhibiting mimetic peroxidase activity of BiO-BDC-NH₂. The possible electrocatalytic mechanism and feasibility of electrochemical determination of total chromium based on BiO-BDC-NH₂/GCE sensor are shown in Fig. 6D.

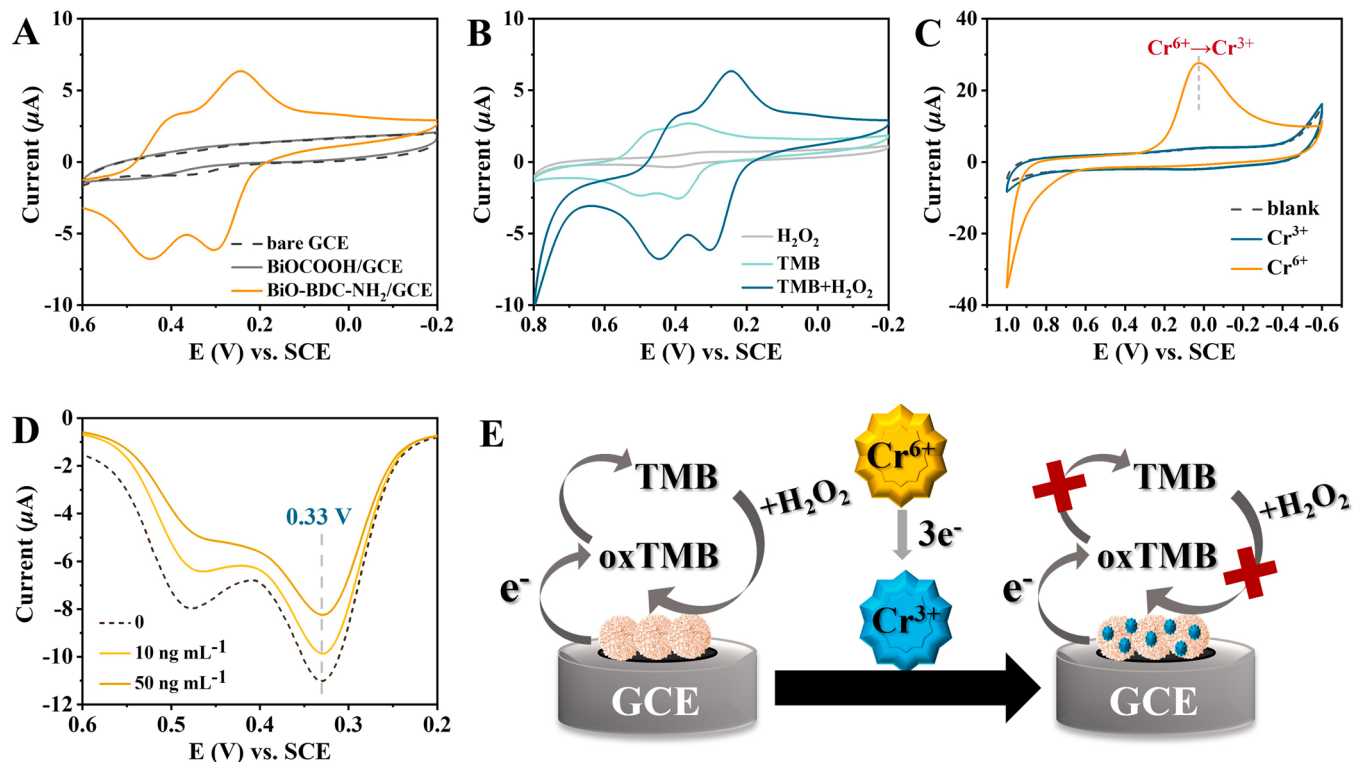


Fig. 6. (A) The comparison of peroxidase-like activity of BiOCOOH and BiO-BDC-NH₂ via CV (0.10 mol L⁻¹ ABS, pH 4.0). (B) CV observation of BiO-BDC-NH₂ peroxidase-like activity. (C) The CV curves of 10 mg L⁻¹ Cr³⁺ and Cr⁶⁺ solutions (0.10 mol L⁻¹ ABS, pH 4.0). (D) The DPV curves of TMB+H₂O₂ system (0.10 mol L⁻¹ ABS, pH 4.0) on BiO-BDC-NH₂/GCE with 10 and 50 ng mL⁻¹ Cr⁶⁺. (Inset plots: Corresponding photographs). (E) Illustration of the electrochemical method of BiO-BDC-NH₂ nanozyme as a probe for Cr⁶⁺ or total chromium detection.

In order to obtain the optimal conditions for electrochemical detection, the main experimental parameters including ABS pH, and the concentration of BiO-BDC-NH₂ nanzyme, TMB and H₂O₂ were investigated. ABS pH could significantly affect the oxidation of TMB and the dissociation of H₂O₂, resulting in a shift in oxidation potential of oxTMB and changes in current. Therefore, the effect of pH on the TMB+H₂O₂ system was first investigated via CV (Fig. S5A). With increasing pH, protons were shown to participate in the oxidation peak potential (Ep) of oxTMB shifted negatively with increasing pH. The linear regression equations for the pH-dependent shift of Ep can be given as two linear: Ep = -0.067 pH + 0.498 ($R^2 = 0.999$) for pH 3.0 – 4.0 and Ep = -0.025 pH + 0.327 ($R^2 = 0.999$) for pH 4.0 – 6.0 (Fig. S5B). According to linear regression equations, each pH unit causes a 67 mV shift in Ep during pH 3.0 – 4.0, which was slightly higher than the theoretical Nernst slope (59.5 mV pH⁻¹), indicating that an electron transfer process dominated by equal numbers of two electrons and two protons [1, 2]. Similar to the colorimetric assay, pH 4.0 ABS was selected for further testing.

The amount of BiO-BDC-NH₂ nanzyme on the electrode surface plays an important role in the electrocatalytic behavior of the sensor. Optimization of the modified amount of BiO-BDC-NH₂ on GCE was investigated by oxTMB oxidation peak current at 0.33 V by varying the concentration of BiO-BDC-NH₂ solution of 0.5 – 3.0 mg mL⁻¹ (Fig. S5C). Maximum oxidation peak currents were observed for modification with 2.5 mg mL⁻¹ BiO-BDC-NH₂ solution, thus 2.5 mg mL⁻¹ BiO-BDC-NH₂ was selected as the optimum for modification on the GCE surface (Fig. S5D). The influence of the TMB substrate on the oxidation peak current was investigated over a concentration range of 0.04–0.36 mmol L⁻¹ (Fig. S5E). As the concentration of TMB increases, the oxidation peak currents gradually increase, reaching the equilibrium value of 0.32 mmol L⁻¹ (Fig. S5F). The concentration of H₂O₂ was optimized from 10.0 to 140 mmol L⁻¹ (Fig. S5G). Peak currents at 0.33 V gradually increase to 120 mmol L⁻¹, and the plot reaches the platform with further increasing concentrations (Fig. S5H). Thus, 0.32 mmol L⁻¹ of TMB and 120 mmol L⁻¹ of H₂O₂ constituted the electrolyte system. The temperature-dependent activity of BiO-BDC-NH₂ was studied (Fig. S5I and J). Under a wide temperature range (4–90 °C), BiO-BDC-NH₂ could remain a stable activity and the following experiment was operated at room temperature.

Under optimized conditions, DPV was applied to analyze the electrochemical performance of the TMB+H₂O₂ system on BiO-BDC-NH₂/GCE with added Cr⁶⁺ concentrations from 0 to 500 ng mL⁻¹. As Cr⁶⁺ concentration increased, oxTMB oxidation peak currents gradually decreased, indicating that the electrochemical sensor was highly dependent on Cr⁶⁺ concentration (Fig. 7A). The response peak current at 0.33 V was plotted as a function of the logarithm value of Cr⁶⁺ concentration and the linear regression equation was I_p (μ A)

= -13.51 + 3.094 log C ($R^2 = 0.990$) (Fig. 7B). Response peak currents were proportional to Cr⁶⁺ at a concentration of 0.30 – 500 ng mL⁻¹, and the detection limit (LOD) was 9.00 ng mL⁻¹ (3 S/N).

Compared to previous reports, the developed dual-model method shows comparable or lower detection limits and linear ranges (Table S2). By this method, the total chromium level can be detected in the form of Cr³⁺, which would be more eco-friendly than Cr⁶⁺ due to the lower toxicity. In addition, most electrochemical analytical procedures are invisible to the naked eye due to changes in analyte concentration at trace/ultra-trace level. While the analysis strategy based on the electroactive TMB+H₂O₂ system involved both electro catalyzing oxidation and chromogenic reactions, which are capable of visual discrimination.

3.6. Peroxidase mimic activity and catalytic analysis of BiO-BDC-NH₂

Peroxidase mimic activity of BiO-BDC-NH₂ nanzyme was verified by reacting with TMB and H₂O₂ substrates. For the colorimetric model, the initial velocity of BiO-BDC-NH₂ nanzyme was defined as the number of moles of TMB or H₂O₂ per mole of catalyst when reacted for 5 min and calculated by Lambert-Beer law (Fig. 8A-B). Typical Lineweaver-Burk double reciprocal plots were constructed from initial velocity versus substrate concentrations (Fig. 8C-D). The K_m and V_{max} of BiO-BDC-NH₂ nanzyme were calculated to be 0.410 mmol L⁻¹ and 5.81 × 10⁻⁵ mmol L⁻¹ s⁻¹ for TMB, and 7.19 mmol L⁻¹ and 3.85 × 10⁻⁵ mmol L⁻¹ s⁻¹ for H₂O₂, respectively. The kinetic parameters of BiO-BDC-NH₂ nanzyme are listed and compared with the reported peroxidase-mimetics (Table S3). In general, the peroxidase-like activity of BiO-BDC-NH₂ nanzyme is comparable to or better than the listed nanomaterials. The affinity of BiO-BDC-NH₂ nanzyme for TMB is strong, which may be due to the preferred bond between the positively charged TMB and the relatively negative BiO-BDC-NH₂ under acidic conditions [9].

Amperometric response curves of the proposed BiO-BDC-NH₂/GCE without and with Cr⁶⁺ pretreatment on successive addition of TMB (Fig. S6A). Peroxidase-mimic catalytic rates were studied according to the response current enhanced by the added concentration of TMB in the presence of various amounts of Cr⁶⁺ (Fig. S6B). The relative linear equations and calculated K_m were shown in Table S4. The double reciprocal lines intersect at origin rather than parallel to each other, and the slopes increase with the increase of Cr⁶⁺ concentration, revealing a typical reversible inhibition effect (Fig. S6C).

BiO-BDC-NH₂ nanzyme energy levels were assessed via CV, and band energy values were estimated with the Mulliken electronegativity theory and calculated by empirical equations [12] (Fig. S7). The conduction band energy (E_{CB}) and valence band energy (E_{VB}) of BiO-BDC-NH₂ nanzyme were calculated as -4.57 eV and 0.40 eV (vs. NHE), respectively, and the energy band gap (E_g) was 4.96 eV.

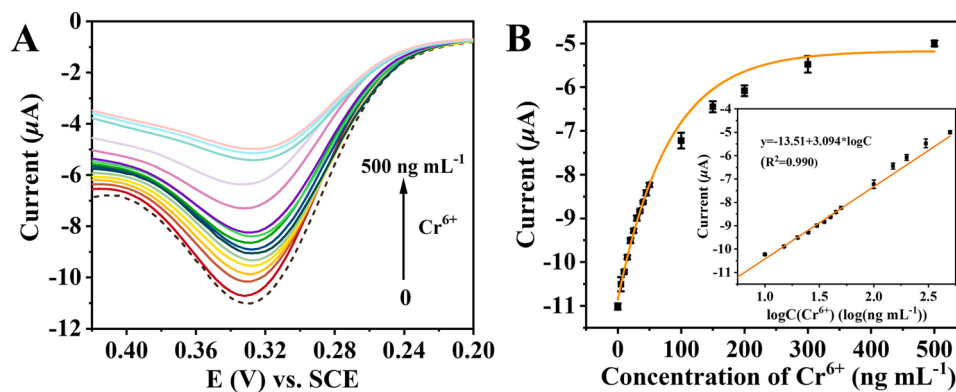


Fig. 7. (A) The superimposed diminishing DPV curves of TMB+H₂O₂ system (0.10 mol L⁻¹ ABS, pH 4.0) on BiO-BDC-NH₂/GCE with increasing concentration of Cr⁶⁺. (B) Linear relationship between response peak current at 0.33 V and the different concentrations of Cr⁶⁺ in the range from 0 to 500 ng mL⁻¹ (Inset plots: calibration curve for log C(Cr⁶⁺) vs. current).

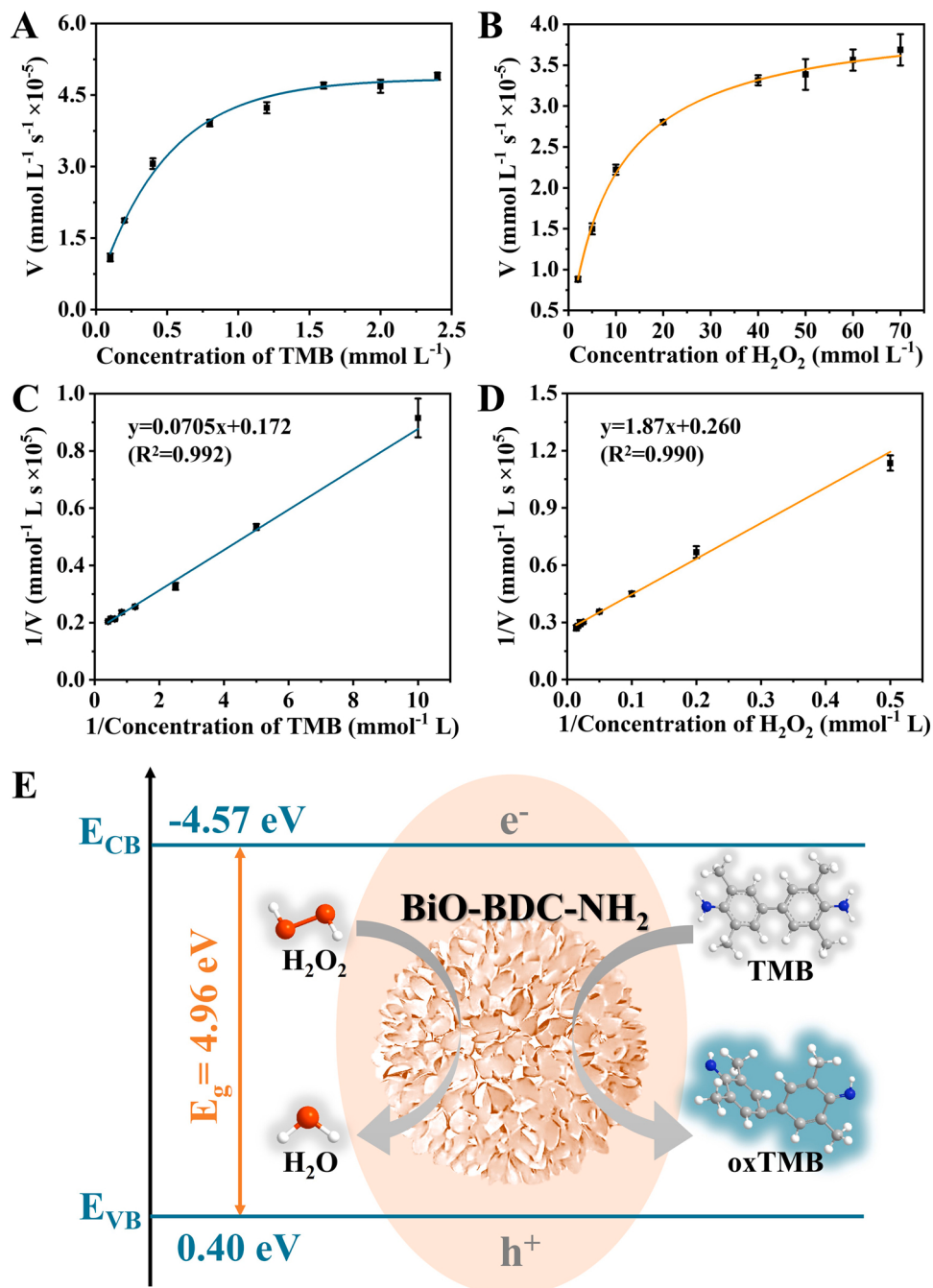


Fig. 8. The results of Michaelis-Menten equation nonlinear fitting on the experimental data from (A) TMB and (B) H₂O₂. The typical Lineweaver-Burk double reciprocal plots of (C) TMB and (D) H₂O₂. (E) The suggested mechanism of BiO-BDC-NH₂ as peroxidase-mimetics for the catalysis to the TMB+H₂O₂ system.

The catalytic oxidation process for TMB and H₂O₂ on BiO-BDC-NH₂ nanzyme can be explained in Fig. 8E. Peroxidase-mimetic activity of BiO-BDC-NH₂ nanzyme follows the typical Michaelis-Menten kinetic and ping-pong mechanism [11]. In the colorimetric system, the large specific surface area of BiO-BDC-NH₂ is available for H₂O₂ absorption and radical •OH production, and surface Bi sites play a dominant role in H₂O₂ activation and TMB oxidation via Fenton or Haber-Weiss reactions [48]. For the electrochemical model, electrons were temporarily stored in the conduction band (CB) of BiO-BDC-NH₂, then transferred to induce the reduction of H₂O₂ and oxidation of TMB. Compared with the colorimetric system, the electrochemical model can accelerate the electron transfer between BiO-BDC-NH₂ nanzyme and electrode and result in rapid catalytic oxidation of TMB in the presence of H₂O₂.

3.7. Selectivity, repeatability and stability of dual-model method

Selectivity experiments of the BiO-BDC-NH₂ nanzyme catalytic TMB+H₂O₂ system towards Cr⁶⁺ (500 ng mL⁻¹) were implemented by testing 100-fold concentration of Cl⁻, NO₃⁻, SO₄²⁻, HCO₃⁻, CO₃²⁻, Na⁺, K⁺, NH₄⁺, Ag⁺, Ca²⁺, Mg²⁺, Ba²⁺, Pb²⁺, Co²⁺, Cd²⁺, Zn²⁺ and Al³⁺, and 10-fold of Hg²⁺, Cu²⁺, Fe²⁺ and Fe³⁺ (Fig. 9A). The relative deviation of the ΔOD_{652} with the addition of other possible interfere ions was 0.64%–16.5%, confirming the observable selectivity of the constructed colorimetric system to Cr⁶⁺.

For the electrochemical model, signal variation was monitored in the TMB+H₂O₂ system absence and presence of 500 ng mL⁻¹ Cr⁶⁺ with 100-fold concentrations of Cl⁻, NO₃⁻, SO₄²⁻, HCO₃⁻, CO₃²⁻, Na⁺, K⁺, NH₄⁺,

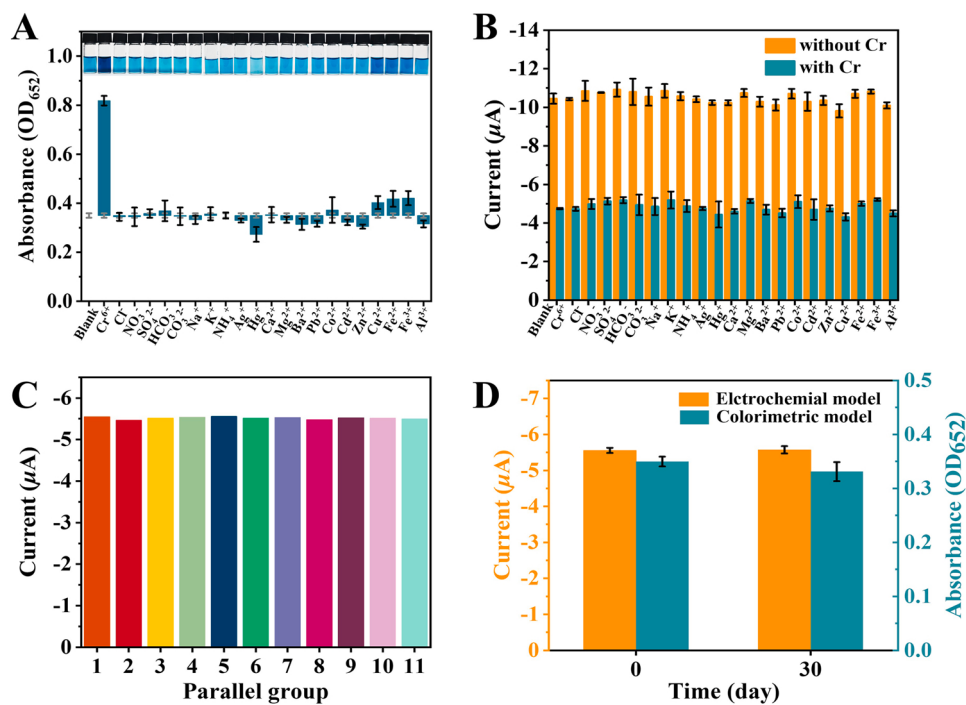


Fig. 9. Comparison of (A) the OD₆₅₂ of the BiO-BDC-NH₂ catalyzed TMB+H₂O₂ system in the presence of the interfering ions (Inset plots: Corresponding photographs) and (B) the oxidation peak currents with/without Cr⁶⁺ on BiO-BDC-NH₂/GCE in the presence interfering ions in TMB+H₂O₂ system. (C) 11 parallel detections on BiO-BDC-NH₂/GCE in TMB+H₂O₂ system. (D) Stability of the BiO-BDC-NH₂ nanozyme stored at 4 °C for 30 days.

Ag⁺, Ca²⁺, Mg²⁺, Ba²⁺, Pb²⁺, Co²⁺, Cd²⁺, Zn²⁺, Fe²⁺, Fe³⁺, Al³⁺, and 10-fold of Cu²⁺ and Hg²⁺ (Fig. 9B). With and without Cr⁶⁺ presence, the relative error of the response current caused by the addition of interfere ions was less than 8.72%, indicating the specific response of the BiO-BDC-NH₂ based electrochemical model to Cr⁶⁺.

The repeatability of the developed BiO-BDC-NH₂/GCE was performed on 11 identical parallel electrodes, and the RSD of the response peak current was 1.24% (Fig. 9C). In addition, the stability of the prepared BiO-BDC-NH₂ nanozyme was evaluated by storing the electrode at 4 °C for 30 days (Fig. 9D). The RSDs of the electrochemical model and colorimetric model were 0.27% and 5.34%, respectively.

3.8. Analytical application

To evaluate the practicability of the developed dual-mode method, Cr⁶⁺ was detected in real samples (drinking water, tap water, lake water and soil), and recovery experiments were adopted for accuracy assessment (Table 1). The amount of Cr⁶⁺ in the drinking water sample was under the LODs of the dual-model method. For tap water, Cr⁶⁺ was only

detected by electrochemical model at 12.1 μg kg⁻¹, which confirmed to the maximum permissible level of Cr⁶⁺ concentration set by WHO at 50.0 μg kg⁻¹ [21]. In lake water and soil samples, the tests of Cr⁶⁺ were positive and the detected amounts were in good agreement with the electrochemical and colorimetric model. The average recoveries of Cr⁶⁺ extract samples were calculated as 91.5%–107.5% by electrochemical method and 92.9%–104.1% by colorimetric method, yielding RSD less than 9.87%.

4. Conclusion

A dual-model method based on BiO-BDC-NH₂ nanozyme was developed for rapid and sensitive detection of Cr⁶⁺. The colorimetric model based on the peroxidase-mimic activity BiO-BDC-NH₂ nanozyme achieved convenient and visual detection at the trace level (LOD: 0.44 ng mL⁻¹). The conversion of the colorimetric model into an eco-friendly and sensitive electrochemical model further improved the detection limit to ultra-trace level (LOD: 9.00 pg mL⁻¹). The synthesized BiO-BDC-NH₂ had excellent catalytic activity, providing an idea for the

Table 1
Results for the determination of Cr⁶⁺ in real samples.

Samples	Electrochemical detection				Colorimetric detection			
	Added (ng mL ⁻¹)	Found (μg kg ⁻¹)	Recovery (%)	RSD (%)	Added (ng mL ⁻¹)	Found (μg kg ⁻¹)	Recovery (%)	RSD (%)
Drinking water	0	ND	-	-	0	ND	-	-
	10	15.5 ± 0.76	98.5	4.92	50	58.0 ± 5.72	104.1	9.87
Tap water	100	97.8 ± 4.08	92.5	4.17	100	136.3 ± 9.17	94.7	6.73
	0	12.1 ± 0.46	-	3.78	0	ND	-	-
Lake water	10	23.3 ± 2.42	105.4	1.04	50	51.9 ± 5.92	96.4	11.4
	100	102.6 ± 5.18	91.5	5.05	100	137.2 ± 8.92	95.3	6.50
Soil	0	116.7 ± 6.54	-	5.60	0	129.8 ± 15.6	-	12.2
	50	156.1 ± 3.51	93.6	2.25	50	168.7 ± 11.8	93.8	6.98
100	213.8 ± 18.6	98.6	8.71	100	235.2 ± 19.9	102.3	8.45	
	0	305.4 ± 28.7	-	9.40	0	329.3 ± 23.1	-	7.00
	50	368.5 ± 30.9	103.7	8.38	50	353.0 ± 23.5	93.1	6.67
100	435.7 ± 24.4	107.5	5.59	100	398.6 ± 31.1	92.9	7.80	

ND: Not detected (below the LOD: 0.44 ng mL⁻¹ for colorimetric detection, 9.00 pg mL⁻¹ for electrochemical detection).

preparation of MOF nanozymes and the utilization of their enzyme-mimic properties. The electrochemical and colorimetric models are complementary, and the developed dual-model method provides a built-in correction to improve detection reliability and can be adapted to detect in a wide linear range and different application scenarios. In future work, it is important to integrate the dual-model method into a portable and convenient device that allows dual signal output simultaneously, and the development of corresponding devices or sensing platforms will have great potential for rapid on-site environmental assays.

Environmental implication

Cr^{6+} is a non-biodegradable heavy metal ion that causes environmental pollution and poses a threat to public health. Herein, a dual-model colorimetric-electrochemical method was conducive to detect trace to ultra-trace Cr^{6+} based on the synthesized BiO-BDC-NH₂ nanozyme with effective peroxidase-mimic activity. The rapid and visual colorimetric model was converted into an electrochemical model with significantly improved Cr^{6+} sensitivity and detection limit. The developed method provides a built-in correction to improve detection reliability and can be adapted to detect in a wide linear range and different application scenarios, and the development of sensing platform has great potential for on-site assay.

CRediT authorship contribution statement

Qiu-Yu Yang: Conceptualization, Methodology, Formal analysis, Investigation, Writing – original draft. **Chao-Qun Wan:** Formal analysis. **Yu-Xin Wang:** Investigation, Data curation. **Xiao-Fang Shen:** Methodology, Formal analysis, Funding acquisition. **Yue-Hong Pang:** Resources, Writing – review & editing, Project administration, Funding acquisition.

Declaration of Competing Interest

The authors declare that they have no known competing financial interests or personal relationships that could have appeared to influence the work reported in this paper.

Data Availability

Data will be made available on request.

Acknowledgements

This work was supported by the National Natural Science Foundation of China (22276077, 21976070, 22076067), and the Fundamental Research Funds for the Central Universities (JUSRP22003).

Appendix A. Supporting information

Supplementary data associated with this article can be found in the online version at [doi:10.1016/j.jhazmat.2023.131148](https://doi.org/10.1016/j.jhazmat.2023.131148).

References

- [1] Ali, M.Y., Alam, A.U., Howlader, M.M.R., 2020. Fabrication of highly sensitive Bisphenol A electrochemical sensor amplified with chemically modified multiwall carbon nanotubes and β -cyclodextrin. *Sens Actuators B Chem* 320. <https://doi.org/10.1016/j.snb.2020.128319>.
- [2] Alves-Balvedi, R.P., Caetano, L.P., Madurro, J.M., Brito-Madurro, A.G., 2016. Use of 3,3',5,5' tetramethylbenzidine as new electrochemical indicator of DNA hybridization and its application in genosensor. *Biosens Bioelectron* 85, 226–231. <https://doi.org/10.1016/j.bios.2016.05.016>.
- [3] Cao, Y., Yue, L., Li, Z., Han, Y., Lian, J., Qin, H., et al., 2023. Construction of Sn-Bi MOF/Ti₃C₂ Schottky junction for photocatalysis of tetracycline: Performance and degradation mechanism. *Appl Surf Sci* 609, 155191. <https://doi.org/10.1016/j.apsusc.2022.155191>.
- [4] Chen, B.-H., Jiang, S.-J., Sahayam, A.C., 2020. Determination of Cr(VI) in rice using ion chromatography inductively coupled plasma mass spectrometry. *Food Chem* 324, 126698. <https://doi.org/10.1016/j.foodchem.2020.126698>.
- [5] Dai, Z., Zhen, Y., Sun, Y., Li, L., Ding, D., 2021. ZnFe₂O₄/g-C₃N₄ S-scheme photocatalyst with enhanced adsorption and photocatalytic activity for uranium (VI) removal. *Chem Eng J* 415, 129002. <https://doi.org/10.1016/j.cej.2021.129002>.
- [6] dos Santos, J.M., Quináia, S.P., Felsner, M.L., 2018. Fast and direct analysis of Cr, Cd and Pb in brown sugar by GF AAS. *Food Chem* 260, 19–26. <https://doi.org/10.1016/j.foodchem.2018.03.106>.
- [7] Duan, F., Zheng, Y., Liu, L., Chen, M., Xie, Y., 2010. Synthesis and photocatalytic behaviour of 3D flowerlike bismuth oxide formate architectures. *Mater Lett* 64, 1566–1569. <https://doi.org/10.1016/j.matlet.2010.04.046>.
- [8] Ejeta, S.Y., Imae, T., 2021. Selective colorimetric and electrochemical detections of Cr(III) pollutant in water on 3-mercaptopropionic acid-functionalized gold plasmon nanoparticles. *Anal Chim Acta* 1152, 338272. <https://doi.org/10.1016/j.aca.2021.338272>.
- [9] Fu, B., Liu, T., Chen, J., Li, K., 2019. CaF₂ nanoparticles as peroxidase mimics for rapid and sensitive detection of aldosterone. *Anal Chim Acta* 1078, 119–124. <https://doi.org/10.1016/j.aca.2019.06.005>.
- [10] Fu, W., Zhang, K., Zhang, X., Fan, G., Wang, Z., Chen, S., et al., 2023. Synthesis of transition metal sulfide functionalized hierarchically porous carbons and their application as colorimetric-electrochemical dual-mode nanozyme sensing platform for dopamine. *Electrochim Acta* 437, 141535. <https://doi.org/10.1016/j.electacta.2022.141535>.
- [11] Gao, L., Zhuang, J., Nie, L., Zhang, J., Zhang, Y., Gu, N., et al., 2007. Intrinsic peroxidase-like activity of ferromagnetic nanoparticles. *Nat Nanotechnol* 2, 577–583. <https://doi.org/10.1038/nnano.2007.260>.
- [12] Guo, X., Yang, F., Jing, L., Li, J., Li, Y., Ding, R., et al., 2022. In-situ generation of highly active and four-in-one CoFe₂O₄/H₂POP nanozyme: Mechanism and its application for fast colorimetric detection of Cr (VI). *J Hazard Mater* 431, 128621. <https://doi.org/10.1016/j.jhazmat.2022.128621>.
- [13] Han, W., Shao, L.-H., Sun, X.-J., Liu, Y.-H., Zhang, F.-M., Wang, Y., et al., 2022. Constructing Cu ion sites in MOF/COF heterostructure for noble-metal-free photoredox catalysis. *Appl Catal B: Environ* 317, 121710. <https://doi.org/10.1016/j.apcatb.2022.121710>.
- [14] Hsu, C.-L., Lien, C.-W., Harroun, S.G., Ravindranath, R., Chang, H.-T., Mao, J.-Y., et al., 2017. Metal-deposited bismuth oxyiodide nanonetworks with tunable enzyme-like activity: sensing of mercury and lead ions. *Mater Chem Front* 1, 893–899. <https://doi.org/10.1039/c6qm00149a>.
- [15] Hu, Z., Xie, X., Li, S., Song, M., Liang, G., Zhao, J., et al., 2021. Rational construct CQDs/BiOCOOH/uCN photocatalyst with excellent photocatalytic performance for degradation of sulfathiazole. *Chem Eng J* 404, 126541. <https://doi.org/10.1016/j.cej.2020.126541>.
- [16] Jayaraman, N., Palani, Y., Jonnalagadda, R.R., Shanmugam, E., 2022. Covalently dual functionalized graphene oxide-based multiplex electrochemical sensor for Hg (II) and Cr(VI) detection. *Sens Actuators B: Chem* 367. <https://doi.org/10.1016/j.snb.2022.132165>.
- [17] Li, S., Chen, J., Jiang, W., Liu, Y., Ge, Y., Liu, J., 2019. Facile construction of flower-like bismuth oxybromide/bismuth oxide formate p-n heterojunctions with significantly enhanced photocatalytic performance under visible light. *J Colloid Interface Sci* 548, 12–19. <https://doi.org/10.1016/j.jcis.2019.04.024>.
- [18] Liang, S., Wu, X.-L., Xiong, J., Yuan, X., Liu, S.-L., Zong, M.-H., et al., 2022. Multivalent Ce-MOFs as biomimetic laccase nanozyme for environmental remediation. *Chem Eng J* 450, 138220. <https://doi.org/10.1016/j.cej.2022.138220>.
- [19] Liu, P., Ptacek, C.J., Blows, D.W., Finfrock, Y.Z., Liu, Y., 2020. Characterization of chromium species and distribution during Cr(VI) removal by biochar using confocal micro-X-ray fluorescence redox mapping and X-ray absorption spectroscopy. *Environ Int* 134, 105216. <https://doi.org/10.1016/j.envint.2019.105216>.
- [20] Liu, X., Wang, F., Meng, Y., Zhao, L., Shi, W., Wang, X., et al., 2022. Electrochemical/visual microfluidic detection with a covalent organic framework supported platinum nanozyme-based device for early diagnosis of pheochromocytoma. *Biosens Bioelectron* 207, 114208. <https://doi.org/10.1016/j.bios.2022.114208>.
- [21] Ma, J., Chen, K., 2020. Designing porous nickel architectures for adsorptive removal of Cr(VI) to achieve drinking water standard. *Sep Purif Technol* 241, 116705. <https://doi.org/10.1016/j.seppur.2020.116705>.
- [22] Ma, Y., Deng, M., Wang, X., Gao, X., Song, H., Zhu, Y., et al., 2022. 2H-MoS₂/Co₃O₄ nanohybrid with type I nitroreductase-mimicking activity for the electrochemical assays of nitroaromatic compounds. *Anal Chim Acta* 1221, 340078. <https://doi.org/10.1016/j.aca.2022.340078>.
- [23] Mädlér, S., Todd, A., "Skip" Kingston, H.M., Pamuku, M., Sun, F., Tat, C., et al., 2016. Ultra-trace level speciated isotope dilution measurement of Cr(VI) using ion chromatography tandem mass spectrometry in environmental waters. *Talanta*, 156–157, 104–111. <https://doi.org/10.1016/j.talanta.2016.04.064>.
- [24] Mao, Y., Gao, S., Yao, L., Wang, L., Qu, H., Wu, Y., et al., 2021. Single-atom nanozyme enabled fast and highly sensitive colorimetric detection of Cr(VI). *J Hazard Mater* 408, 124898. <https://doi.org/10.1016/j.jhazmat.2020.124898>.
- [25] Mei, L., Zhu, S., Liu, Y., Yin, W., Gu, Z., Zhao, Y., 2021. An overview of the use of nanozymes in antibacterial applications. *Chem Eng J* 418, 129431. <https://doi.org/10.1016/j.cej.2021.129431>.

- [26] Monga, A., Fulke, A.B., Dasgupta, D., 2022. Recent developments in essentiality of trivalent chromium and toxicity of hexavalent chromium: Implications on human health and remediation strategies. *J Hazard Mater Adv* 7, 100113. <https://doi.org/10.1016/j.jhazadv.2022.100113>.
- [27] Motaghedifard, M.H., Pourmortazavi, S.M., Mirsadeghi, S., 2021. Selective and sensitive detection of Cr(VI) pollution in waste water via polyaniline/sulfated zirconium dioxide/multi walled carbon nanotubes nanocomposite based electrochemical sensor. *Sens Actuators B: Chem* 327, 128882. <https://doi.org/10.1016/j.snb.2020.128882>.
- [28] Paithankar, J.G., Saini, S., Dwivedi, S., Sharma, A., Chowdhuri, D.K., 2021. Heavy metal associated health hazards: An interplay of oxidative stress and signal transduction. *Chemosphere* 262, 128350. <https://doi.org/10.1016/j.chemosphere.2020.128350>.
- [29] Pang, Y.-H., Huang, Y.-Y., Wang, L., Shen, X.-F., Wang, Y.-Y., 2020. Determination of bisphenol A and bisphenol S by a covalent organic framework electrochemical sensor. *Environ Pollut* 263, 1373. <https://doi.org/10.1016/j.envpol.2020.114616>.
- [30] Pang, Y.H., Yang, Q.Y., Jiang, R., Wang, Y.Y., Shen, X.F., 2022. A stack-up electrochemical device based on metal-organic framework modified carbon paper for ultra-trace lead and cadmium ion detection. *Food Chem* 398, 133822. <https://doi.org/10.1016/j.foodchem.2022.133822>.
- [31] Qin, G., Niu, Z., Yu, J., Li, Z., Ma, J., Xiang, P., 2021. Soil heavy metal pollution and food safety in China: Effects, sources and removing technology. *Chemosphere* 267, 129205. <https://doi.org/10.1016/j.chemosphere.2020.129205>.
- [32] Saraiva, M., Chekri, R., Leufroy, A., Guérin, T., Sloth, J.J., Jitaru, P., 2021. Development and validation of a single run method based on species specific isotope dilution and HPLC-ICP-MS for simultaneous species interconversion correction and speciation analysis of Cr(III)/Cr(VI) in meat and dairy products. *Talanta* 222, 121538. <https://doi.org/10.1016/j.talanta.2020.121538>.
- [33] Spanu, D., Monticelli, D., Bindà, G., Dossi, C., Rampazzi, L., Recchia, S., 2021. One-minute highly selective Cr(VI) determination at ultra-trace levels: An ICP-MS method based on the on-line trapping of Cr(III). *J Hazard Mater* 412, 125280. <https://doi.org/10.1016/j.jhazmat.2021.125280>.
- [34] Tan, F., Cong, L., Jiang, X., Wang, Y., Quan, X., Chen, J., et al., 2017. Highly sensitive detection of Cr(VI) by reduced graphene oxide chemiresistor and 1,4-dithiothreitol functionalized Au nanoparticles. *Sens Actuators B Chem* 247, 265–272. <https://doi.org/10.1016/j.snb.2017.02.163>.
- [35] Tang, Y., Jiang, S., Li, W., Jalil Shah, S., Zhao, Z., Pan, L., et al., 2022. Confined construction of COF@Cu-nanozyme with high activity and stability as laccase biomimetic catalyst for the efficient degradation of phenolic pollutants. *Chem Eng J* 448, 137701. <https://doi.org/10.1016/j.cej.2022.137701>.
- [36] Tu, J., Gan, Y., Liang, T., Wan, H., Wang, P., 2018. A miniaturized electrochemical system for high sensitive determination of chromium(VI) by screen-printed carbon electrode with gold nanoparticles modification. *Sens Actuators B Chem* 272, 582–588. <https://doi.org/10.1016/j.snb.2018.06.006>.
- [37] Unnikrishnan, B., Lien, C.W., Chu, H.W., Huang, C.C., 2021. A review on metal nanozyme-based sensing of heavy metal ions: Challenges and future perspectives. *J Hazard Mater* 401, 123397. <https://doi.org/10.1016/j.jhazmat.2020.123397>.
- [38] Wang, C., Shang, M., Wei, H., Zhang, M., Zou, W., Meng, X., et al., 2021. Specific and sensitive on-site detection of Cr(VI) by surface-enhanced Raman spectroscopy. *Sens Actuators B Chem* 346, 130594. <https://doi.org/10.1016/j.snb.2021.130594>.
- [39] Wang, H., Chen, T., Chen, D., Zou, X., Li, M., Huang, F., et al., 2020. Sulfurized oolitic hematite as a heterogeneous Fenton-like catalyst for tetracycline antibiotic degradation. *Appl Catal B Environ* 260, 118203. <https://doi.org/10.1016/j.apcatb.2019.118203>.
- [40] Wang, J., Huang, R., Qi, W., Su, R., He, Z., 2022. Preparation of amorphous MOF based biomimetic nanozyme with high laccase- and catecholase-like activity for the degradation and detection of phenolic compounds. *Chem Eng J* 434, 134677. <https://doi.org/10.1016/j.cej.2022.134677>.
- [41] Wei, L., Li, Q., Li, H., Ye, H., Han, D., Guo, Z., et al., 2022. Speciation-specific Cr bioaccumulation, morphologic and transcriptomic response in liver of *Plectropomus leopardus* exposed to dietary Cr(III) and Cr(VI). *Ecotoxicol Environ Saf* 241, 113744. <https://doi.org/10.1016/j.ecoenv.2022.113744>.
- [42] Welch, C.M., Nekrassova, O., Compton, R.G., 2005. Reduction of hexavalent chromium at solid electrodes in acidic media: reaction mechanism and analytical applications. *Talanta* 65, 74–80. <https://doi.org/10.1016/j.talanta.2004.05.017>.
- [43] Wen, S.H., Zhong, X.L., Wu, Y.D., Liang, R.P., Zhang, L., Qiu, J.D., 2019. Colorimetric assay conversion to highly sensitive electrochemical assay for bimodal detection of arsenate based on cobalt oxyhydroxide nanozyme via arsenate absorption. *Anal Chem* 91, 6487–6497. <https://doi.org/10.1021/acs.analchem.8b05121>.
- [44] Wise Jr., J.P., Young, J.L., Cai, J., Cai, L., 2022. Current understanding of hexavalent chromium [Cr(VI)] neurotoxicity and new perspectives. *Environ Int* 158, 106877. <https://doi.org/10.1016/j.envint.2021.106877>.
- [45] Xing, J., Li, J., Yang, F., Fu, Y., Huang, J., Bai, Y., et al., 2022. Cyclic enrichment of chromium based on valence state transformation in metal-free photocatalytic reductive imprinted composite hydrogel. *Sci Total Environ* 839, 156367. <https://doi.org/10.1016/j.scitotenv.2022.156367>.
- [46] Xu, H., Zeng, L., Huang, D., Xian, Y., Jin, L., 2008. A Nafion-coated bismuth film electrode for the determination of heavy metals in vegetable using differential pulse anodic stripping voltammetry: An alternative to mercury-based electrodes. *Food Chem* 109, 834–839. <https://doi.org/10.1016/j.foodchem.2007.12.065>.
- [47] Yang, J., Sun, Y., Wang, Z., Gong, J., Gao, J., Tang, S., et al., 2022. Heavy metal pollution in agricultural soils of a typical volcanic area: Risk assessment and source appointment. *Chemosphere* 304, 135340. <https://doi.org/10.1016/j.chemosphere.2022.135340>.
- [48] Yang, W., Yang, X., Zhu, L., Chu, H., Li, X., Xu, W., 2021. Nanozymes: activity origin, catalytic mechanism, and biological application. *Coord Chem Rev* 448, 214170. <https://doi.org/10.1016/j.ccr.2021.214170>.
- [49] Yu, K., Li, M., Chai, H., Liu, Q., Hai, X., Tian, M., et al., 2023. MOF-818 nanozyme-based colorimetric and electrochemical dual-mode smartphone sensing platform for in situ detection of H₂O₂ and H₂S released from living cells. *Chem Eng J* 451, 138321. <https://doi.org/10.1016/j.cej.2022.138321>.
- [50] Yu, L., Pang, Y., Mo, Z., Huang, Y., Shen, X., 2021. Coordination array for accurate colorimetric sensing of multiple heavy metal ions. *Talanta* 231, 122357. <https://doi.org/10.1016/j.talanta.2021.122357>.
- [51] Zhang, Q., Fu, Y., Xiao, K., Du, C., Zhang, X., Chen, J., 2021. Sensitive dual-mode biosensors for CYFRA21-1 assay based on the dual-signaling electrochemical ratiometric strategy and “On-Off-On” PEC method. *Anal Chem* 93, 6801–6807. <https://doi.org/10.1021/acs.analchem.1c00746>.
- [52] Zhang, X., Zhi, H., Zhu, M., Wang, F., Meng, H., Feng, L., 2021. Electrochemical/visual dual-readout aptasensor for Ochratoxin A detection integrated into a miniaturized paper-based analytical device. *Biosens Bioelectron* 180, 113146. <https://doi.org/10.1016/j.bios.2021.113146>.
- [53] Zheng, W., Lee, L.Y.S., 2021. Metal-organic frameworks for electrocatalysis: catalyst or precatalyst. *ACS Energy Lett* 6, 2838–2843. <https://doi.org/10.1021/acsenergylett.1c01350>.